

## Distinct predatory behaviors in scimitar- and dirk-toothed sabertooth cats

Figueirido, Borja; Lautenschlager, Stephan; Pérez-Ramos, Alejandro; Van Valkenburgh, Blaire

DOI:

[10.1016/j.cub.2018.08.012](https://doi.org/10.1016/j.cub.2018.08.012)

License:

Creative Commons: Attribution-NonCommercial-NoDerivs (CC BY-NC-ND)

*Document Version*

Peer reviewed version

*Citation for published version (Harvard):*

Figueirido, B, Lautenschlager, S, Pérez-Ramos, A & Van Valkenburgh, B 2018, 'Distinct predatory behaviors in scimitar- and dirk-toothed sabertooth cats', *Current Biology*, vol. 28, no. 20, pp. 3260–3266.e3. <https://doi.org/10.1016/j.cub.2018.08.012>

[Link to publication on Research at Birmingham portal](#)

### **Publisher Rights Statement:**

Checked for eligibility: 21/11/2018

### **General rights**

Unless a licence is specified above, all rights (including copyright and moral rights) in this document are retained by the authors and/or the copyright holders. The express permission of the copyright holder must be obtained for any use of this material other than for purposes permitted by law.

- Users may freely distribute the URL that is used to identify this publication.
- Users may download and/or print one copy of the publication from the University of Birmingham research portal for the purpose of private study or non-commercial research.
- User may use extracts from the document in line with the concept of 'fair dealing' under the Copyright, Designs and Patents Act 1988 (?)
- Users may not further distribute the material nor use it for the purposes of commercial gain.

Where a licence is displayed above, please note the terms and conditions of the licence govern your use of this document.

When citing, please reference the published version.

### **Take down policy**

While the University of Birmingham exercises care and attention in making items available there are rare occasions when an item has been uploaded in error or has been deemed to be commercially or otherwise sensitive.

If you believe that this is the case for this document, please contact [UBIRA@lists.bham.ac.uk](mailto:UBIRA@lists.bham.ac.uk) providing details and we will remove access to the work immediately and investigate.

1 **Three-dimensional biomechanics reveals distinct predatory behaviors in scimitar- and**  
2 **dirk-toothed sabertooth cats**

3

4 Borja Figueirido<sup>1\*</sup>, Stephan Lautenschlager<sup>2</sup>, Alejandro Pérez-Ramos<sup>1</sup> and Blaire Van  
5 Valkenburgh<sup>3</sup>

6

7 <sup>1</sup>Universidad de Málaga, Departamento de Ecología y Geología, Facultad de Ciencias, 29071-  
8 Málaga, Spain.

9 <sup>2</sup>School of Geography, Earth and Environmental Sciences, University of Birmingham,  
10 Edgbaston, Birmingham, B15 2TT, UK.

11 <sup>3</sup>Department of Ecology and Evolutionary Biology, UCLA, 621 Charles E Young Drive South,  
12 Los Angeles, CA 90095-1606.

13

14 \*author for corresponding: Borja.figueirido@uma.es

15

16 **Keywords:** cranial biomechanics, cortical bone, trabecular bone, finite element analysis,  
17 paleobiology, killing bite, dirk-teeth, scimitar-teeth

18

19 **SUMMARY**

20 Over the Cenozoic, large cat-like forms have convergently evolved into specialized killers of  
21 ‘megaherbivores’ that relied on their large, and laterally-compressed (saber-like) canines to  
22 rapidly subdue their prey [1-5]. Scimitar- and dirk-toothed sabertooths are distinct ecomorphs  
23 that differ in canine tooth length, degree of serration, and postcranial features indicative of

24 dissimilar predatory behavior [6-13]. Despite these differences, it is assumed that they used a  
25 similar ‘canine-shear’ bite to drive their sabers through their prey [14,15]. We investigated the  
26 killing behavior of the scimitar-toothed *Homotherium serum* and the dirk-toothed *Smilodon*  
27 *fatalis* using a comparative sample of living carnivores and a new quantitative approach to the  
28 analysis of skull function. For the first time, we quantified differences in the relative amount and  
29 distribution of cortical (CB) and trabecular bone (TB) in coronal sections of skulls to assess  
30 relative skull stiffness and flexibility [16-19]. We also use finite element analysis to simulate  
31 various killing scenarios that load skulls in ways that are likely to favor distinct proportions of  
32 CB/TB across the skull. Our data reveal that *S. fatalis* had an extremely thick skull and relatively  
33 little TB, consistent with a large investment in cranial strength for a stabbing canine-shear-bite.  
34 However, *H. serum* had more TB, and likely deployed an unusual predatory behavior that was  
35 more similar to the clamp-and-hold technique of the lion than *S. fatalis*. These data broaden the  
36 killing repertoire of sabertooths and highlight the degree of ecological specialization among  
37 members of the large carnivore guild during the Late Pleistocene of North America.

38

## 39 **RESULTS**

### 40 *Profiles of CB and TB*

41 As CB tends to have high stiffness and TB has greater flexibility [16-19], we hypothesize that if  
42 dirk-tooths and scimitar-tooths had distinctive killing bites that loaded their skulls differently,  
43 they should diverge in the quantity and distribution of CB/TB as well. To test this, we quantified  
44 the relative amount of cortical (CB) and trabecular bone (TB) of complete skulls of the two  
45 sabertooths and three extant large carnivores, African lion (*Panthera leo*), spotted hyena  
46 (*Crocuta crocuta*), and African wild dog (*Lycaon pictus*) (Fig. 1A; see methods for justification

47 of comparative sample). Our results reveal that the skulls of all species show two clear peaks in  
48 CB surface area relative to the total area of the skull (RCBT) to varying degrees with the  
49 exception of the wild dog (Fig. 1B, left). The first lies at the upper fourth premolar (carnassial),  
50 and the second at the temporomandibular joint (TMJ). In the wild dog, the peak at the carnassial  
51 is not pronounced, and CB area increases more gradually across the skull than in the feliforms  
52 (Fig. 1B, left). Across all five species, there is considerable variation in the distribution of CB  
53 surface area across the skull, with *S. fatalis* exceeding all species in the snout (slices #1-5;  
54 Fig. 1B; Fig. 2) except at the anterior-most point of the upper carnassial, where it is surpassed by  
55 the spotted hyena (slice #3; Fig. 1B). The snout of *H. serum* has values of relative CB area that  
56 are below those of *S. fatalis* except at slices #1 and #5, the anterior-most point of the canine and  
57 the posterior-most point of the upper carnassial, respectively. Between those two positions, the  
58 snout of *H. serum* is more similar to that of the extant lion in relative compact bone surface area  
59 and much less than observed in the hyena and *S. fatalis*. (Fig. 1B, left). Beyond slice #5, both  
60 saber-tooths have similar values of CB that fall below those of the wild dog and hyena  
61 posteriorly (slices #5-10; Fig. 1B).

62 On a per slice basis, the proportion of CB (RCBS) fluctuates across the skull in all five  
63 species, with all showing a decline at the TMJ (slice#8, Fig. 1C, left). Within the snout, the  
64 proportion of CB per slice is greatest in the spotted hyena and *S. fatalis*, and least in the lion and  
65 *H. serum* (Fig. 1C, left). Interestingly, the snout of the wild dog is similar to that of the spotted  
66 hyena and *S. fatalis* in the proportion of compact bone at two anterior locations (slices #2-3), but  
67 then declines for the remainder of the snout (slices #4-5; Fig. 1C, left).

68 TB surface area relative to total skull area (RTBT) in *S. fatalis* is most similar to that of  
69 the spotted hyena, and to a lesser extent, *H. serum* and the wild dog (Fig. 1B, right). The lion

70 stands out with an unusually large proportion of TB at the TMJ (slice #8, Fig. 1B; Fig. 2) as well  
71 as higher values at both the posterior margin of the upper carnassial/frontal region and behind the  
72 TMJ (slices #4-5, 9-10; Fig 1B). The relatively large proportion of TB in the lion is confirmed in  
73 the analysis of TB area per slice (RTBS), in which the lion displays an exceptionally large  
74 proportion of TB per slice at the TMJ and caudal most position. (slice #8, 10, Fig. 1C). On a per  
75 slice basis, the values for *H. serum* are also elevated and similar to those of the lion within the  
76 anterior-most part of the snout (slices # 1-3; Fig. 1C). However, posteriorly (slices # 4-10; Fig.  
77 1B), *H. serum* has relative TB area per slice values within the range of *S. fatalis* and all extant  
78 species except the lion (slices # 5-10; Fig. 1B).

79

#### 80 *Finite element analysis*

81 We used 3D biomechanical modelling to simulate a variety of killing scenarios, such as  
82 stabbing or pulling back, that load skulls differently and therefore are likely to favor distinct  
83 proportions of CB/TB across the skull. Biomechanical function and efficiency were assessed via  
84 von Mises stress and displacement magnitudes in the different models/scenarios. Von Mises  
85 stress is a scalar function of principal stresses (along orthogonal planes) and is a good predictor  
86 of ductile material failure (20), whereas displacement magnitude indicates the deformation of  
87 individual elements/regions due to external loading.

88 A comparison of von Mises stress values for each species under the four different loading  
89 scenarios reveals that the skulls of the three felids undergo less stress during stabbing bites than  
90 the skulls of either *Crocota* or *Lycaon* (blue line, Fig. 3A). Of the three felids, *S. fatalis* exhibits  
91 the least stress during a stabbing bite, followed closely by *H. serum* and then the lion. However,

92 average values of node displacements under a stabbing load are very similar for both sabertooths  
93 (Fig. 3B).

94 Contour plots of von Mises stress distributions reveal notable differences between *S.*  
95 *fatalis* and *H. serum* during bilateral canine stabbing and pulling back. During bilateral canine  
96 stabbing, both sabertooths are similar in showing relatively high stress across their braincase but  
97 differ anteriorly, with *S. fatalis* exhibiting less stress across the rostrum than *H. serum* (Fig. 4).  
98 However, the situation is different during the pull-back scenario, in which both show similar  
99 stress in the rostrum but *S. fatalis* has greater stress across the braincase and zygomatics than *H.*  
100 *serum*. All three of the extant species experience higher stresses during bilateral canine stabbing  
101 than either of the saber-tooths (Fig. 4).

102 Mean von Mises stress values in *S. fatalis* (Fig. 3A) under laterally directed extrinsic  
103 loads (lateral shake) are greater than in any other simulated scenario, and exceed those observed  
104 for either *H. serum* or the lion. In both the lion and *H. serum*, the stresses are similar and the  
105 laterally directed extrinsic forces largely concentrate von Mises stress around the zygomatics and  
106 the rostral region (Fig. 4). However, average values of node displacement under lateral shake  
107 loads indicate that *H. serum* experiences considerably lower displacements than the lion or *S.*  
108 *fatalis* (Fig. 3B).

109 All the taxa experience lower average von Mises stress values with a jaw-muscle-driven  
110 bite (Fig. 3A), but this is particularly true for the skull of *C. crocuta* and *L. pictus* (Fig. 3A).  
111 Stresses are lower in this scenario than the others because the primary forces are distributed  
112 across the braincase and posterior half of the skull, and the rostrum is relatively unaffected (Fig.  
113 4). In contrast, because the extrinsic scenarios have a higher load focus on the anterior half of the

114 skull, the skulls are more prone to bending under the simulated loads, especially in elongated  
115 skulls.

116

## 117 **DISCUSSION**

118 Cortical bone (CB) differs from trabecular bone (TB) in having a higher Young's  
119 modulus, and therefore, a high supportable load per unit of surface area. However, it has a lower  
120 strain index, which gives it greater stiffness and greater ability to resist torque (16-19).

121 Therefore, the large amount of CB in the rostrum of *S. fatalis* (Fig. 1B; Fig. 2) indicates that,  
122 similar to the bone-cracking spotted hyena, it was especially equipped to resist larger and more  
123 localized stresses than the rostra of both the living *P. leo* (Fig. 1B; Fig. 2) and the scimitar-  
124 toothed *H. serum* (Fig. 1B; Fig. 2). In fact, the three-dimensional simulations of different killing-  
125 bite scenarios reveal that the rostrum of *S. fatalis* was better able to withstand loads induced  
126 when stabbing prey than that of *H. serum* (Fig. 4). Moreover, within our sample of five large  
127 carnivorans, the skull of *S. fatalis* is the only one that exhibits a lesser displacement under a  
128 stabbing scenario than under a lateral-shake scenario (Fig. 3B).

129 Contrary to CB, TB has a lower Young's modulus, and the supportable load per unit of  
130 surface area is reduced, but TB has a higher strain index that gives it greater flexibility (16-19).  
131 Moreover, TB is better than CB in resisting compression and shear (16-19). Accordingly, TB is  
132 25% as dense, 10% as stiff, and 500% as ductile as CB (16-19). The small proportion of TB in  
133 the skull of *S. fatalis* (Fig. 1B, C; Fig. 2), particularly in the posterior region, suggests that its  
134 skull was not optimized for resisting sustained, multidirectional and large loads imposed by  
135 struggling prey (Fig. 3; Fig. 4). As demonstrated by previous researchers (e.g., 21), *S. fatalis*  
136 probably used its powerfully-built forelimbs (10,22) with hypertrophied dew claws (23,24) to

137 bring down and fully immobilize large prey, and then applied one or two quick, strong killing-  
138 bites to the throat (e.g., 1,2, 7, 13, 14, 25, 26).

139 In contrast, the large amount of TB in the posterior region of the skull of *P. leo* (Fig.  
140 1B,C; Fig. 2) reflects its ability to resist the continuous and repetitive multidirectional loads that  
141 might occur during a prolonged ‘clamp-and-hold’ bite (27,28). Results of the FEA analyses also  
142 support the idea that the skulls of lions are better adapted to resist laterally-directed loads than  
143 those of the sabertooths. For example, although the skulls of *P. leo* and *H. serum* exhibit a  
144 similar level of stress when simulating a lateral-shake scenario (Fig. 3A), the rostrum of *P. leo* is  
145 less stressed, above the canines (Fig. 4). Moreover, whereas the skull of *H. serum* experiences  
146 slightly lower levels of stress under a stabbing than a lateral-shake scenario (Fig. 3A), the skull  
147 of *P. leo* experiences similar levels under both scenarios (Fig. 3A), and the average skull  
148 displacement of *P. leo* was much lower under a lateral-shake than a stabbing scenario (Fig. 3B).

149 The rostrum of *H. serum* exhibits an intermediate amount of CB to those of *S. fatalis* and  
150 *P. leo* (Fig. 1B,C; Fig. 2), suggesting that the skull of *H. serum* had an intermediate ability to  
151 resist high peaks of locally concentrated and unidirectional forces. This is consistent with the  
152 results obtained from biomechanical simulations of bilateral canine stabbing, in which *H. serum*  
153 experienced levels of stress in between that observed in *S. fatalis* and the three extant taxa (Fig.  
154 3B; Fig. 4).

155 On the other hand, as the skull of *H. serum* was also in between both *S. fatalis* and *P. leo*  
156 in quantity of TB (Fig. 1B,C), its ability to resist continuous and multidirectional loads also  
157 should be intermediate to these two felids. Again, the biomechanical simulations for different  
158 prey-killing scenarios support this because the skull of *H. serum* and the lion display similar



159 overall levels of stress under a lateral-shake scenario, and considerably less than *S. fatalis* (Fig.  
160 3A; Fig. 4).

161 Our results suggest that *H. serum* deployed a predatory behavior among large felids, not  
162 previously supported with quantitative data, that was in between the canine-shear-bite of *S.*  
163 *fatalis* (or dirktooths in general) and the clamp-and-hold technique of lions (or conical teeth).  
164 We argue that, like *S. fatalis*, multiple debilitating slashing bites onto the throat of large prey was  
165 the most likely predatory behavior for *H. serum*, and probably for all scimitar-tooths, as  
166 originally proposed by previous researchers based on qualitative assessments of morphology  
167 (e.g., 7). However, unlike *S. fatalis*, our results suggests that the skull of *H. serum* was less  
168 stressed by laterally directed loads, which is consistent with a predatory behavior that regularly  
169 subjected the skull to such loads as observed in the lion. In support of this, an analysis of upper  
170 canine tooth bending strength in carnivorans found that the canines of *H. serum* were more  
171 resistant to bending and presumably fracture under mediolaterally directed loads than were the  
172 canines of *S. fatalis* (29).

173 The skull of the scimitar-tooth *H. serum* likely was able to support multidirectional loads  
174 incurred by struggling prey more often than was *S. fatalis* because of profound differences in  
175 their forelimb morphology. Scimitar-tooths were somewhat cursorial predators in open habitats,  
176 whereas dirk-tooths behaved as ambush predators in more closed environments (11).  
177 Consequently, the forelimbs of *H. serum* exhibit greater adaptations for speed, while those of *S.*  
178 *fatalis* emphasize adaptations for strength. Relative to *S. fatalis*, *H. serum* had less robust humeri  
179 (diameter/length), less broad humeral epicondyles, relatively shorter olecranon processes and a  
180 longer radius to humerus ratio, all of which are consistent with a reduced mechanical advantage  
181 of the forelimb muscles and less muscle mass (30). In addition, although the claws of *H. serum*

182 are compressed and curve-shaped, those of digits II-V are reduced and less retractile than those  
183 of *S. fatalis*, indicating an adaptive trade-off in the scimitar tooth between having improved  
184 traction for pursuing prey and enhanced grappling ability (31). All of these forelimb  
185 characteristics suggest less of a reliance on the forelimbs for immobilization of the prey than was  
186 the case for *S. fatalis*, and consequently a need for a craniodental skeleton better equipped to  
187 support lateral shaking (12). Therefore, our results suggest a gradient of potential functional  
188 adaptations in a group of highly specialized predators from the clamp-and-hold technique of the  
189 living lion through *H. serum* to the exceedingly specialized canine-shear-bite of *S. fatalis*.

190 Finally, we note that our analysis of cortical and trabecular bone thickness and  
191 distribution in these five carnivorans revealed a previously unrecognized and unique feature of *S.*  
192 *fatalis*. Based on the specimen we scanned, *S. fatalis* had an extremely thick skull as evidenced  
193 by the coronal sections as well as our quantitative measures (Fig. 1). The combined thickness of  
194 CB and TB, as well as CB alone, in the rostrum far exceeds that of any the other four species. At  
195 the temporomandibular joint, *S. fatalis*, *H. serum* and the spotted hyena exhibit greater total bone  
196 thickness than the lion, and unlike the lion, much of this thickness is CB rather than TB. Spotted  
197 hyenas are capable of cracking large bones with their strong teeth and jaws, and their massive  
198 TMJ likely reflects the associated high bite forces (32, 33). Similarly, the extraordinary thickness  
199 of the skull of *S. fatalis* in both the rostrum and TMJ suggests an exceptionally large investment  
200 in cranial strength in *S. fatalis*, and argues for extremely high bite forces in this cat. Therefore,  
201 although both the CB/TB and FE analyses are conducted in a single specimen and might not  
202 represent the pattern for the entire species, our results support clear differences in predatory  
203 behavior between the scimitar-tooth *H. serum*, and the dirk-tooth *S. fatalis*. In future work, we  
204 plan to take advantage of the large sample of *S. fatalis* from the Rancho La Brea tar seeps to

205 explore intraspecific and ontogenetic variability in skull morphology and strength. In addition,  
206 given that previous studies have revealed profound interspecific differences among saber-tooth  
207 locomotory and predatory strategies among (34), future studies including more species of living  
208 felines and other recognized species of *Smilodon* and *Homotherium*, such as their South  
209 American vicars, *Smilodon populator* (35) and *Homotherium venezuelensis* (36), could provide  
210 additional insights into the diversity of cranial biomechanics in this group of extinct mammalian  
211 predators.

212

### 213 **ACKNOWLEDGMENTS**

214 We are grateful to Digimorph team, especially to Jessie Maisano for kindly providing the CTs  
215 analyzed in this study. Three anonymous reviewers provided very helpful comments on the  
216 manuscript. Funding for this project was provided by the ‘Spanish Ministry of Economy and  
217 Competitiveness (MINECO), grant (CGL2015-58300P) to BF. APR is a FPI fellow of the  
218 Spanish MINECO (BES-2013-065469) associated to the project (CGL2012-37866) of BF.

219

### 220 **AUTHOR CONTRIBUTIONS:**

221 B.F., B.V.V. designed research; A. P.-R., B.F., S.L., B.V.V. performed research; B.F., B.V.V.,  
222 A.P.-R., S.L., wrote the paper.

223 The authors declare no conflict of interest.

224

### 225 **REFERENCES**

- 226 1. Bohlin, B. (1940). Food habit of the machaerodonts, with special regard to *S. fatalis*.  
227 Bull. Geol. Inst. Upsala 28, 156-174.

- 228 2. Emerson, S.B., and Radinsky, L. (1980). Functional analysis of sabertooth cranial  
229 morphology. *Paleobiology* 6, 295-312.
- 230 3. Van Valkenburgh, B. (2007). Deja vu: the evolution of feeding morphologies in the  
231 Carnivora. *Integr. Comp. Biol.* 47, 147-163.
- 232 4. Andersson, K., Norman, D., and Werdelin, L. (2011). Sabretoothed carnivores and the  
233 killing of large prey. *PLoS One* 6, e24971.
- 234 5. Palmqvist, P., Martínez-Navarro, B., and Arribas, A. (1996). Prey selection by terrestrial  
235 carnivores in a lower Pleistocene paleocommunity. *Paleobiology* 22, 514-534.
- 236 6. Kurtén, B. (1968). *Pleistocene Mammals of Europe*. Weidenfeld and Nicolson,  
237 London.
- 238 7. Martin, L.D. (1980). Functional morphology and the evolution of cats. *Transactions of*  
239 *the Nebraska Academy of Sciences* 8, 141-154.
- 240 8. Slater, G.J., and Van Valkenburgh, B. (2008). Long in the tooth: evolution of sabertooth  
241 cat cranial shape. *Paleobiology* 34, 403-419.
- 242 9. Martin, L.D., Babiarez, J.P., Naples, V.L., and Hearst, J. (2000). Three ways to be a saber-  
243 toothed cat. *Naturwissenschaften* 87, 41-44.
- 244 10. Meachen-Samuels, J.A., and Van Valkenburgh, B. (2010). Radiographs reveal  
245 exceptional forelimb strength in the sabertooth cat, *S. fatalis fatalis*. *PLoS one* 5, e11412.
- 246 11. Anyonge, W. (1996). Locomotor behaviour in Plio-Pleistocene sabre-tooth cats: a  
247 biomechanical analysis. *J. Zool.* 238, 395-413.
- 248 12. Antón, M. (2013). *Sabertooth*. Indiana University Press.
- 249 13. Gonyea, W. J. (1976) Behavioral implications of saber-toothed felid morphology.  
250 *Paleobiology* 2, 332-342.

- 251 14. Akersten, W.A. (1985). Canine function in *S. fatalis* (Mammalia; Felidae;  
252 machairodontinae). Natural History Museum of Los Angeles County, Contributions in  
253 Science, 356.
- 254 15. Antón, M., and Galobart, A. (1999). Neck function and predatory behavior in the scimitar  
255 toothed cat *H. serum latidens* (Owen). J. Vertebr. Paleontol. 19, 771-784.
- 256 16. Carter, D.R., and Hayes, W.C. (1977). Compact bone fatigue damage—I. Residual  
257 strength and stiffness. J. Biomech. 10: 325-337.
- 258 17. Guede, D., González, P., and Caeiro, J.R. (2013). Biomecánica y hueso (I): Conceptos  
259 básicos y ensayos mecánicos clásicos. Revista de Osteoporosis y Metabolismo Mineral 5,  
260 43-50.
- 261 18. Reddy, S., Dischino, M., and Soslowsky, L.J. (2009). Biomechanics-Part I. Bone  
262 Pathology, ed. Khurana J (Humana Press, New York), pp. 61-68.
- 263 19. Mostakhdemin, M., Amiri, I.S., and Syahrom, A. (2016). Introduction of Bone Study.  
264 Multi-axial Fatigue of Trabecular Bone with Respect to Normal Walking, eds.  
265 Mostakhdemin M, Amiri IS, Syahrom (Springer Singapore), pp. 1-4.
- 266 20. Dumont, E. R., Piccirillo, J., & Grosse, I. R. (2005). Finite-element analysis of biting  
267 behavior and bone stress in the facial skeletons of bats. *The anatomical record*, 283(2),  
268 319-330.
- 269 21. McHenry, C.R., Wroe, S., Clausen, P.D., Moreno, K., and Cunningham, E. (2007).  
270 Supermodeled sabercat, predatory behavior in *S. fatalis fatalis* revealed by high-  
271 resolution 3D computer simulation. P. Natl. Acad. Sci. USA 104, 16010-16015.
- 272 22. Martín-Serra, A., Figueirido, B., and Palmqvist, P. (2017). Non-decoupled morphological  
273 evolution of the fore-and hindlimb of sabretooth predators. J. Anat. 231, 532-542.

- 274 23. Cox, M., and Jefferson, G.T. (1988). The first individual skeleton of *S. fatalis* from  
275 Rancho La Brea. *Current Research in the Pleistocene* 5, 66-67.
- 276 24. Bryant, H.N., Russell, A.P., Laroia, R., and Powell, G.L. (1996). Claw retraction and  
277 protraction in the Carnivora: skeletal microvariation in the phalanges of the Felidae. *J.*  
278 *Morphol.* 229, 289-308.
- 279 25. Antón, M., Salesa, M.J., Pastor, J.F., Sanchez, I.M., Fraile, S., and Morales, J. (2004).  
280 Implications of the mastoid anatomy of larger extant felids for the evolution and  
281 predatory behaviour of sabretoothed cats (Mammalia, Carnivora, Felidae). *Zool. J. Linn.*  
282 *Soc.-Lond.* 140, 207-221.
- 283 26. Salesa, M.J., Antón, M., Turner, A., and Morales, J. (2005). Aspects of the functional  
284 morphology in the cranial and cervical skeleton of the sabre-toothed cat  
285 *Paramachairodus ogygia* (Kaup, 1832) (Felidae, Machairodontinae) from the Late  
286 Miocene of Spain: implications for the origins of the machairodont killing bite. *Zool. J.*  
287 *Linn. Soc.-Lond.* 144, 363-377.
- 288 27. Schaller, G.B. (2009). *The Serengeti lion: a study of predator-prey relations*. University  
289 of Chicago Press.
- 290 28. Sunquist, M., and Sunquist, F. (2017). *Wild cats of the world*. University of Chicago  
291 Press.
- 292 29. Valkenburgh, B.V., and Ruff, C.B. (1987). Canine tooth strength and killing behaviour in  
293 large carnivores. *J. Zool.* 212, 379-397.
- 294 30. Meachen-Samuels, J.A. (2012). Morphological convergence of the prey-killing arsenal of  
295 sabertooth predators. *Paleobiology* 38, 1-14.

- 296 31. Antón, M., Galobart, A., and Turner, A. (2005). Co-existence of scimitar-toothed cats,  
297 lions and hominins in the European Pleistocene. Implications of the post-cranial anatomy  
298 of *H. serum latidens* (Owen) for comparative palaeoecology. *Quaternary Sci. Rev.* 24,  
299 1287-1301.
- 300 32. Kruuk, H. (1972). *The Spotted Hyena* a study of predation and social behavior. Chicago;  
301 Univ. Of Chicago Press.
- 302 33. Ravosa, M.J., Kunwar, R., Stock, S.R., and Stack, M.S. (2007). Pushing the limit:  
303 masticatory stress and adaptive plasticity in mammalian craniomandibular joints. *J.*  
304 *Experimental Biology* 210, 628-641.
- 305 34. Lewis, M.E., and Lague, MR. (2010). Interpreting sabertooth cat (Carnivora; Felidae;  
306 Machairodontinae) postcranial morphology in light of scaling patterns in felids.  
307 *Carnivoran evolution: new views on phylogeny, form and function.* Cambridge  
308 University Press, Cambridge, 411.
- 309 35. Lund, P.W. 1842. Blik paa Brasiliens Dyreverden för sidste Jordomvaeltning. Fjerde  
310 Afhandling: Forstsættelse af Pattedyrene. *Danke vidensk. Selsk.*, 9:137-209.
- 311 36. Rincón, A. D., Prevosti, F. J., & Parra, G. E. (2011). New saber-toothed cat records  
312 (Felidae: Machairodontinae) for the Pleistocene of Venezuela, and the Great American  
313 Biotic Interchange. *Journal of Vertebrate Paleontology*, 31(2), 468-478.
- 314 37. Marinelli, W. (1938). Der Schlidel von *S. fatalis*, nach der Funktion das Kieferapparates  
315 analysiert. *Paleobiologica* 6, 246-272.
- 316 38. Rawn-Schatzinger, V. (1992). The scimitar cat, *H. serum serum* cope: osteology,  
317 functional morphology, and predatory behavior. Illinois State Museum.
- 318 39. Marean, C.W., and Ehrhardt, C.L. (1995). Paleoanthropological and paleoecological  
319 implications of the taphonomy of a sabertooth's den. *J. Hum. Evol* 29, 515-547.

- 320 40. Antón, M., Salesa, M.J., Galobart, A., and Tseng, Z. J. (2014). The Plio-Pleistocene  
321 scimitar-toothed felid genus *H. serum* Fabrini, 1890 (Machairodontinae, Homotherini):  
322 diversity, palaeogeography and taxonomic implications. *Quaternary Sci. Rev.* 96: 259-  
323 268.
- 324 41. Schneider, C.A., Rasband, W.S., and Eliceiri, K.W. (2012). NIH Image to ImageJ: 25  
325 years of image analysis. *Nat. methods* 9, 671-675.
- 326 42. Kikinis, R., Pieper, S.D., and Vosburgh, K.G. (2014). 3D Slicer: a platform for subject-  
327 specific image analysis, visualization, and clinical support. *Intraoperative imaging and*  
328 *image-guided therapy*, ed, Jolesz FA (Springer New York), pp. 277-289.
- 329 43. Lehmann, L.A., Alvarez, R.E., Macovski, A., Brody, W.R., Pelc, N.J., Riederer, S.J., and  
330 Hall, Al. (1981). Generalized image combinations in dual KVP digital radiography. *Med.*  
331 *Phys.* 8, 659-667.
- 332 44. Ney, D. R., Fishman, E. K., Magid, D., and Drebin, R.A. (1990). Volumetric rendering of  
333 computed tomography data: Principles and techniques. *IEEE Computer Graphics and*  
334 *Applications.* 10, 24-32.
- 335 45. Sezgin, M., and Sankur, B. (2004). Survey over image thresholding techniques and  
336 quantitative performance evaluation. *J. Electron Imaging* 13, 146-165.
- 337 46. Cignoni, P., Callieri, M., Corsini, M., Dellepiane, M., Ganovelli, F., and Ranzuglia, G.  
338 (2008). Meshlab: an open-source mesh processing tool. *Eurographics Italian Chapter*  
339 *Conference:* 129-136.
- 340 47. Chamoli, U., and Wroe, S. (2011). Allometry in the distribution of material properties  
341 and geometry of the felid skull: Why larger species may need to change and how they  
342 may achieve it. *Journal of Theoretical Biology*, 283(1), 217-226.



- 343 48. Slater, G. J., and Van Valkenburgh, B. (2009). Allometry and performance: the evolution  
344 of skull form and function in felids. *J. Evolution. Biol.* 22, 2278-2287.
- 345 49. Attard, M.R.G., Chamoli, U., Ferrara, T.L., Rogers, T.L., and Wroe, S. (2011). Skull  
346 mechanics and implications for feeding behaviour in a large marsupial carnivore guild:  
347 the thylacine, Tasmanian devil and spotted-tailed quoll. *J. Zool.* 285, 292-300.
- 348 50. Bourke, J., Wroe, S., Moreno, K., McHenry, C., & Clausen, P. (2008). Effects of gape  
349 and tooth position on bite force and skull stress in the dingo (*Canis lupus dingo*) using a  
350 3-dimensional finite element approach. *PLoS One*, 3(5), e2200.
- 351 51. Thomason, J.J. (1991). Cranial strength in relation to estimated biting forces in some  
352 mammals. *Can. J. Zool.* 69, 2326-2333.
- 353 52. Rayfield, E.J. (2007). Finite element analysis and understanding the biomechanics and  
354 evolution of living and fossil organisms. *Annu. Rev. Earth Planet. Sci.* 35, 541-576.

355

356

357

358 **Figure 1.** Amount and distribution of cortical (CB) and trabecular bone (TB). A, *S. fatalis* skull  
359 (left); palatal view of theseskull showing the positions of the ten coronal slices selected for  
360 quantifying the area of CB and TB (middle), and representative slice taken at position #8, the  
361 temporomandibular joint (right), with CB in yellow and TB in green. B, Bivariate plots of  
362 cortical bone area relative to total skull area (RCBT) and trabecular bone area relative to total  
363 skull area (RTBT) across the ten coronal slices. C, Bivariate plots of cortical bone area relative to  
364 total skull area per slice (RCBS), and trabecular bone area relative to total skull area per slice  
365 (RTBS) across the ten coronal slices. The ten slices are: 1, anterior-most point of the canine; 2,

366 posterior-most point of the canine; 3, anterior-most point of the fourth upper premolar; 4,  
 367 junction between the metacone and paracone of the upper fourth premolar; 5, posterior-most  
 368 point of the fourth upper premolar; 6, anterior-most point of the squamosal-jugal suture on the  
 369 zygomatic arch; 7, posterior-most point of the squamosal-jugal suture on the zygomatic arch; 8,  
 370 temporomandibular joint (TMJ); 9, anterior-most point of the tympanic bulla; 10, anterior-most  
 371 point of the occipital condyles. The slices defined at interdental gaps are taken at alveolar  
 372 margins. All the skulls are scaled isometrically to 200 mm from prosthion to inion.

373

374

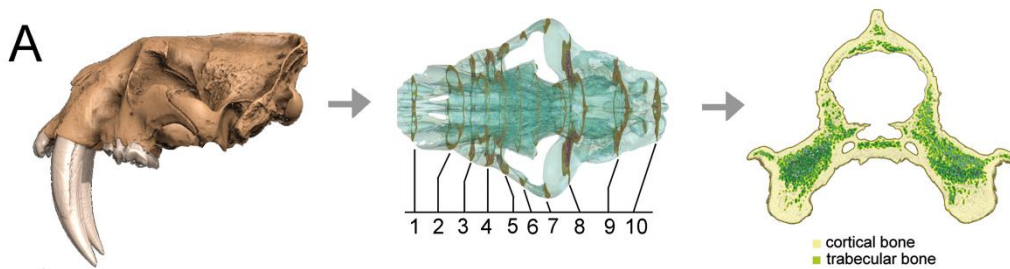
375

376

377

378

379



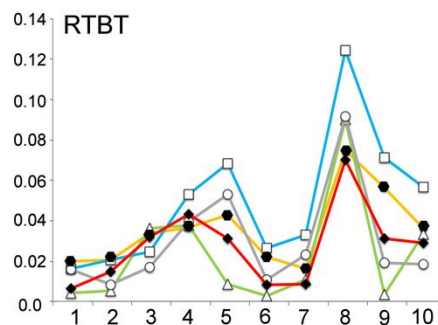
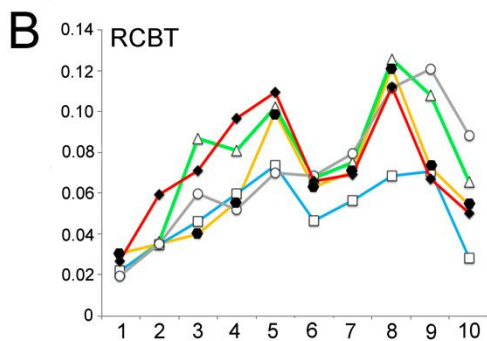
380

381

382

383

384

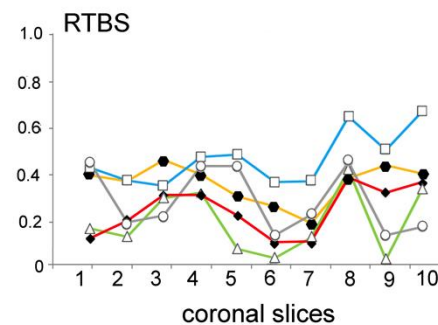
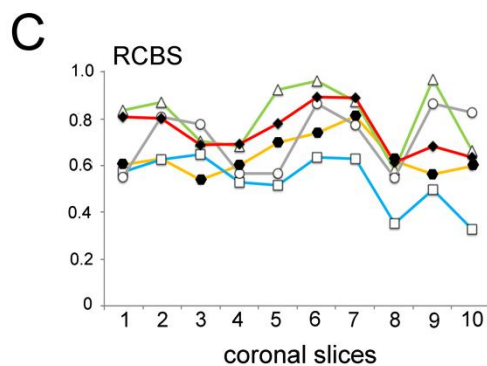


385

386

387

388



◆ *S. fatalis* ● *H. serum* □ *P. leo* ▲ *C. crocuta* ○ *L. pictus*

389 **Figure 2.** Selected coronal slices in the five large carnivores included in the sample scaled to the  
390 same maximum mediolateral width. A, the dirk-toothed *S. fatalis fatalis*; B, the conical-toothed  
391 *Panthera leo*; C, the scimitar-toothed, *H. serum serum*; D, the spotted hyaena *Crocota crocuta*;  
392 E, the African wild dog *Lycaon pictus*. Left shows coronal slice # 3, and right shows coronal  
393 slice #8. Cortical bone, yellow; trabecular bone, green.

394

395

396

397

398

399

400

401

402

403

404

405

406

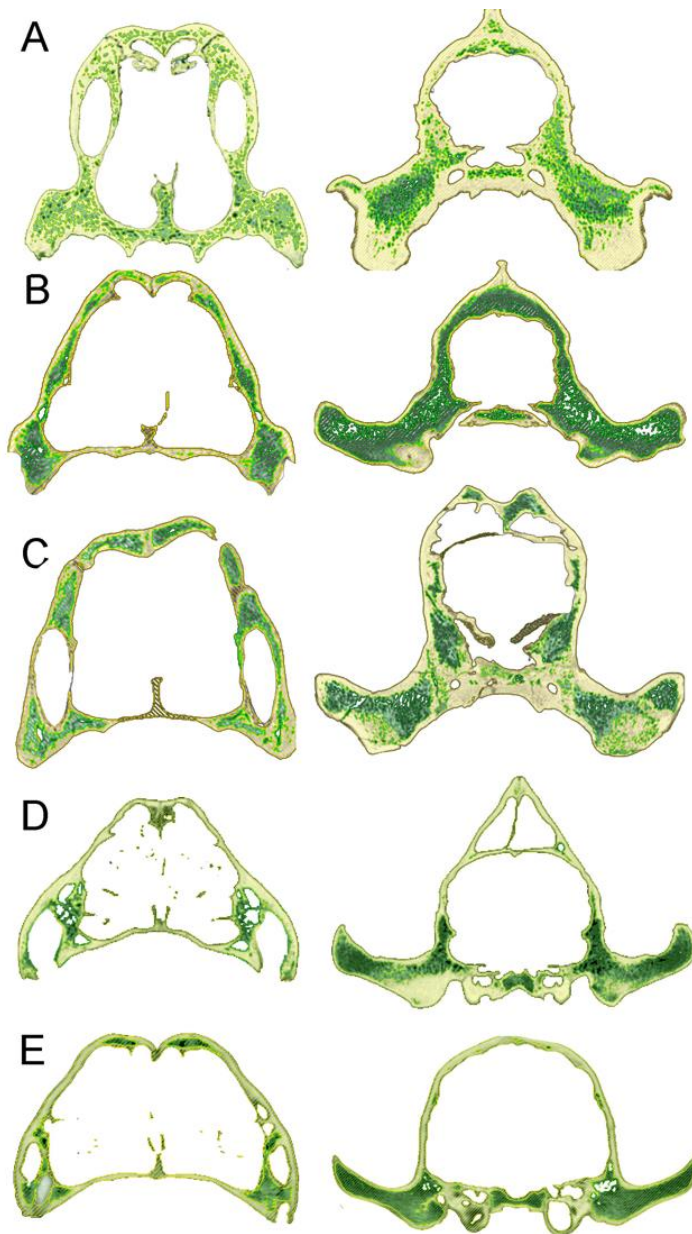
407

408

409

410

411



412 **Figure 3.** Finite Element Analysis. A, average (per element) von Mises stress (MPa) for each  
 413 species in a given loading scenario. B, Average nodal displacement (mm) of the models for each  
 414 species in a given loading scenario as a proxy for model deformation. Data are for models under  
 415 extrinsic and intrinsic loads during bilateral canine biting.

416

417

418

419

420

421

422

423

424

425

426

427

428

429

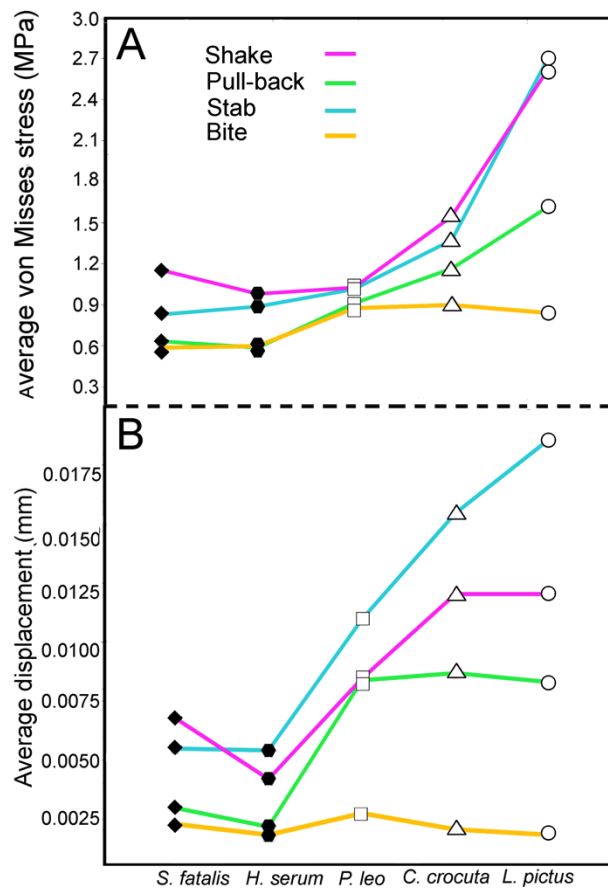
430

431

432

433

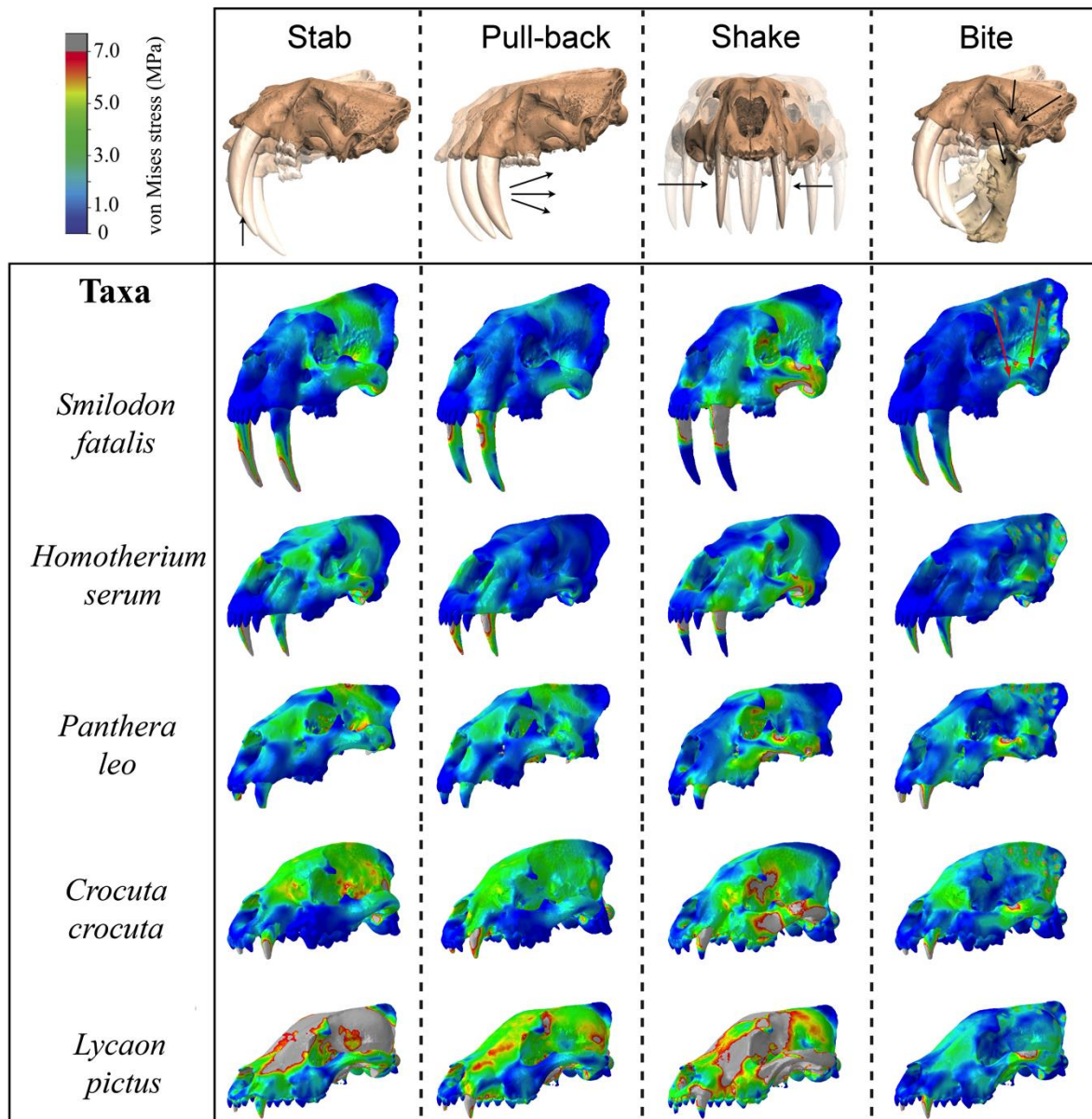
434



435 **Figure 4.** Von Mises stress contour plots obtained from Finite Element Analysis of the crania of  
 436 both sabertooths and living carnivores under four loading conditions (stabbing, pull-back, lateral  
 437 shake, and jaw-powered bite) during bilateral canine biting. See also Figure S2 for the  
 438 simulations of the extrinsic scenarios including the adductor muscles and a fifth intrinsic  
 439 scenario considering jaw adductors plus neck muscles. In Figure S3 the results under unilateral  
 440 canine biting are shown.

441

442



454 **STAR METHODS**

455

456 **Acquisition of CT scans**

457         The crania of the two extinct felids, *H. serum* and *S. fatalis*, as well as three extant  
458 carnivorans, African lion (*Panthera leo*), African wild dog (*Lycaon pictus*), and spotted hyena  
459 (*Crocuta crocuta*) were CT scanned. All specimens were adults as indicated by fully closed  
460 synchondroses and complete tooth eruption. The three extant hypercarnivorous taxa were chosen  
461 because researchers have proposed that *H. serum* was more of a carrion-feeder than lion-like  
462 active predator (37-39), whereas others have suggested *H. serum* was more similar to pack-  
463 hunting canids (12) based on its more gracile limbs and lack of fully retractile claws (31, 40).  
464 All specimens were scanned at the University of Texas High-Resolution X-ray Computed  
465 Tomography Facility and the scans are available on the UT Digital Morphology website ([www.digimorph.org](http://www.digimorph.org)).  
466

467         Both saber-teeth were scanned at the University of Texas High-Resolution X-ray CT  
468 (Facility Archive 1478 for *H. serum* and Facility Archive 0860 for *S. fatalis*). The acquisition  
469 properties for *H. serum* were 1024x1024 pixel size for 16-bit TIFF images, 419 kV, 1.8 mA,  
470 with voxel size (mm) of 0.1904 (X), 0.1904 (Y), 0.6500(Z) (total slices = 495). The acquisition  
471 properties for *S. fatalis* were 1024x1024 16-bit TIFF images, 420 kV, 1.8 mA, with voxel size in  
472 mm of 0.2143(X), 0.2143 (Y), 0.5000 (Z) (total slices = 629). The specimen of *S. fatalis*  
473 (LACMRLP R37376) is from from Rancho La Brea (Los Angeles, California) collected at pit 91,  
474 and *H. serum* at (TMM 933-3444) was discovered at Friesenhahn cave (Texas, USA).

475         We also used extant taxa for comparative purposes, as follows: (i) lion *Panthera leo*  
476 (MVZ 117849) of unknown sex as a large pantherine, specimen collected from Skukuza (Kruger

477 Park, Tranvaal, South Africa), and scanned at the University of Texas High-Resolution X-ray CT  
478 (Facility Archive 0320), acquisition properties were 512x512 16-bit TIFF images of the whole  
479 skull, 420 kV, 1.8 mA, and the voxel size in mm was 0.5273(X), 0.5273 (Y), 1.0000 (Z) (total  
480 slices = 406); (ii) spotted hyena, *Crocuta crocuta* (UCMVZ 184551) as a bone-cracker model, a  
481 male collected from Masai Mara National Reserve, Kenya, and scanned at the University of  
482 Texas High-Resolution X-ray CT (Facility Archives 0277), acquisition properties were 512x512  
483 16-bits and converted 8 bits TIFF images, 420 kV, 1.8 mA, with a voxel size in mm of  
484 0.3242(X), 0.3242 (Y), 0.5000 (Z) (total slices = 528); (iii) African wild dog, *Lycaon pictus*  
485 (USNM 368441), as a pack-hunter hypercarnivore, a male collected in Bechuanaland,  
486 Makeleapudi, and scanned at the University of Texas High-Resolution X-ray CT, acquisition  
487 properties are 1024x1024 16-bit TIFF images, 419 kV, 1.8 mA, (total slices = 523).

488         Museum abbreviations are as follows: Museum of Vertebrate Zoology at Berkley (MVZ);  
489 University of California Museum of Vertebrate Zoology (UCMVZ); United States National  
490 Museum of Natural History at Washington DC (USNM); Los Angeles County Museum, Rancho  
491 La Brea (LCMRLP); and Texas Memorial Museum (TMM).

492

### 493 **Quantification and distribution of CB vs TB**

494         The dataset for each of the scanned skulls consisted of a stack of 16-bit TIFF images, all  
495 of which were adjusted for brightness and contrast to eliminate background noise using ImageJ  
496 (41). All images were normalized at 0.5% and the histogram was adjusted to the range of interest  
497 (ROI) using the semiautomatic brightness/contrast tool of ImageJ (41). Subsequently, all images  
498 were converted to 8 bits and exported to 3D-slicer (42) to generate the 3D models of each skull.  
499 To select the total amount of bone, and to avoid possible overestimations due to Compton and

500 photoelectric effects (43), we used a range of gray values of 70-255 and created a slice with all  
501 the bone. Subsequently, we manually added to this layer the relevant low density structures  
502 (e.g.,TB) using a range of grey values between 40-70. We decided to use this range of gray  
503 values in order to reach a compromise between capturing all the visible and very small  
504 trabeculae but avoiding: (i) the oversegmentation of this relevant bony structures; and (ii) the  
505 selection of other undesirable artifacts that are a result of Compton and Photoelectric effects; and  
506 (iii) the selection of non-relevant small particles. This resulted in a layer with all the information  
507 selected between 40-255 but excluding the background noise due to Compton and photoelectric  
508 effects (40). Using this layer, we then segmented CB and TB, respectively, as those structures  
509 with gray values ranging from approximately 185-255 for CB and 40-185 for TB.

510 For each 3D model of a skull, we selected ten 1-mm thick coronal slices at key points that  
511 were homologous in all the species (Fig. 1A). CB and TB were segmented in each of these ten  
512 slices excluding petrosal bones and teeth, based on the values of thresholding specified above  
513 using 3D-slicer (42). Thus, for each slice, we generated three independent layers, first for all  
514 bone, second for the cortical bone (yellow), and third for trabecular bone (green). Each layer was  
515 saved as a stack of TIFF images to be imported into imageJ (41). All the CTs were processed  
516 using a bicubic interpolation (44) in order to convert anisotropic voxels (in Z direction) to  
517 isotropic-sized voxels (the same X,Y,Z values). Afterwards, the stacks for each skull were scaled  
518 to a total length of 200 mm from prosthion to inion isometrically and oriented to the same plane  
519 in imageJ (41). After converting the stacks into binary, we used the plug-in of ImageJ, ‘analysing  
520 particles’ (45) to obtain the total surface area of CB and TB (including intratrabeuclar spaces),  
521 respectively, in each slice.



522 For both fossil specimens, we used semi-automatic thresholding to select the grey values  
523 corresponding to the matrix (non-bony) material prior to selecting the ten coronal slices. The  
524 values for this thresholding varies across slices and depends upon the nature of matrix infilling.  
525 After selecting the slices, we manually segmented them to remove matrix still present inside the  
526 trabecular bone of the skull. Damaged trabeculae during the fossilization process in the skulls of  
527 both saber-teeth were not observed. Furthermore, the inclusion of the intra-trabecular spaces in  
528 the calculation of TB avoids possible (but not visible), very small damaged trabeculae.  
529 Therefore, there is not an appreciable potential impact of diagenesis on accuracy of measures of  
530 CB and TB in both fossil skulls. Mirroring to compensate for missing structures was done in  
531 only a few instances. The exceptions were a few struts of the frontal sinus in *S. fatalis*, and a  
532 small portion of the palate of *H. serum*, that were restored by mirroring the preserved  
533 counterparts. Restored parts of the skull had a minimum potential impact on the calculation of  
534 CB and TB across the skulls.

535 Both three-dimensional surface models were imported into MeshLab (46) in PLY or STL  
536 formats (Polygon File Format or the Stanford Triangle Format) for mesh repair, cleaning and  
537 simplification.

538 Values of CB and TB were scaled by: i) the sum of CB and TB of the ten slices (i.e., total  
539 area of bone quantified across the skulls); and (ii) the total area of CB plus TB of each slice.  
540 Both approaches are complementary in the following way: the first approach shows not only the  
541 distribution of CB and TB across the skull, but also the heterogeneous distribution of bone across  
542 slices; with the second approach the contribution of CB or TB in each slice is shown without  
543 regard to the heterogeneous distribution of bone across the skull.

544 The proportion of cortical to trabecular bone tends to decrease with increasing size  
545 among felids (47). Therefore, larger species have less cortical bone and more trabecular bone.  
546 However, this allometric effect does not affect our results, given that we analyzed the  
547 distribution of cortical and trabecular bone across ten functional key points of the skull, rather  
548 than just the total amounts of CB and TB. Moreover, both *H. serum* (skull length=326mm) and  
549 *S. fatalis* (skull length=322mm) have similar skull sizes to the living lion (skull length=408 mm),  
550 and yet they vary greatly in CB/TB across their skulls.

551

## 552 **Finite Element Analysis**

553 The 3D models of all skulls were imported into Hypermesh 11 (Altair Engineering) for  
554 the generation of solid meshes (consisting of approximately 1,000,000 tetrahedral elements per  
555 model) and the setting of boundary conditions. All skull models were scaled to the same surface  
556 area to allow comparisons of form and function independent of size (48). Material properties for  
557 bone and teeth were assigned in Hypermesh based on published values in comparable studies on  
558 mammalian carnivores (bone:  $E = 13.7$  (cortical) &  $9.29$  (trabecular) GPa,  $\nu = 0.30$ , teeth:  $E =$   
559  $38.6.0$  GPa,  $\nu = 0.4$ ) (46-48). All materials were treated as isotropic and homogenous.

560 Five different functional scenarios were tested. Three extrinsic scenarios: (i) stabbing  
561 prey using both canine teeth with a dorsally directed extrinsic force of 500 N applied to the tips  
562 of both canines (stab in Figure 4); (ii) pulling the head posteriorly with both canine teeth  
563 embedded in the prey and an extrinsic force of 500 N distributed over the posterior edge of the  
564 canines (pull-back in Figure 4); and (iii) shaking the head laterally while holding prey with both  
565 canine teeth and an extrinsic force of 500 N applied to the left side of both canines (shake in Fig.  
566 4). The extrinsic force (total of 1000 N for each scenario) was selected based on reported

567 magnitudes for neck-muscle-driven bite force (21). For the extrinsic feeding scenarios,  
568 constraints were placed on the articular surface of the squamosal (five nodes on each side), as  
569 well as the occipital condyle (ten nodes) to restrain the model from movement in x-, y- and z-  
570 directions to simulate the fixed contact of the skull with other skeletal elements (i.e. mandible  
571 and vertebral column).

572 A further intrinsic scenario (iv) was analyzed that simulated a jaw adductor muscle-  
573 driven biting assuming a gape angle of 25 degrees following (50). For this purpose, jaw adductor  
574 muscle forces were estimated using the attachment area of each muscle (Fig. S1), as a proxy for  
575 physiological cross-section area and multiplying it by an isometric muscle stress value of 0.3 N/  
576 mm<sup>2</sup> (51). This approach likely underestimates the total muscle force and resulting bite forces  
577 due to simplifying a three-dimensional muscle volume to a two-dimensional surface area.

578 However, given the lack of accurate data on muscle volume and architecture for fossil  
579 carnivorans, this approach provides a repeatable method for estimating muscle force across taxa  
580 and permits functional comparisons. Models in this scenario were constrained at the tip of the  
581 canine tooth (one node on each side) to restrain the model from movement in x- and y- direction  
582 (i.e. medial/lateral and anterior/posterior), but not in z-direction to simulate some penetration of  
583 the canines into the prey during biting.

584 In addition, a combined functional scenario (v) was tested simulating the simultaneous  
585 action of the jaw closing muscles and the neck musculature. For this, an extrinsic force of 500 N  
586 on each side was added to the aforementioned intrinsic scenario and distributed over the back of  
587 the skull and the mastoid region. The magnitude of the load was selected to be the same as with  
588 the extrinsic scenarios, based on reported magnitudes for neck-muscle-driven bite force (21). The  
589 directions of the muscle forces were determined by creating vectors between the muscle origin

590 and insertion sites, using corresponding mandibular models or simplified templates, where this  
591 was not possible (i.e. postcranial muscles).

592 Further to these scenarios and to simulate the combined action of the jaw adductor  
593 muscles and external forces (i.e., stab, pull-back, lateral shake) experienced during movement of  
594 the prey and/or the head, all extrinsic scenarios were further analyzed with adductor loads active.  
595 Cranial (adductor) and postcranial muscles were considered separately in the functional analyses  
596 to evaluate their contribution to the stress behavior. However, combined loads of the cranial and  
597 postcranial musculature were tested as well (see supplementary Figure S2). Results show that the  
598 combined muscle forces have very little effect on the stress distribution. The simulations were  
599 performed during bilateral (Figs. 3,4) and unilateral (Fig. S3) canine biting. All models were  
600 subsequently imported into Abaqus 6.14.1 (Simulia) for analysis and post-processing.

601 Biomechanical performance for the FE models was assessed via contour plots of Von Mises  
602 stress distribution, reaction forces, and average Von Mises stress and displacement values per  
603 element with the top 1% of values removed to avoid the influence of individual stress  
604 singularities at constrained or loaded nodes. The jaw-joint reaction forces quantify the internal  
605 force generated at node constraints (TMJ), the Von Mises (VM) stress distributions represent a  
606 function that measures how stress distorts a material, and the displacement values per element  
607 measure how the elements of the mesh are displaced when a given force is applied (52).